The Astrophysical Journal Letters, 847:L21 (7pp), 2017 October 1 https://doi.org/10.3847/2041-8213/aa8db8

Dispersive Evolution of Nonlinear Fast Magnetoacoustic Wave Trains

D. J. Pascoe, C. R. Goddard, and V. M. Nakariakov
Centre for Fusion, Space and Astrophysics, Department of Physics, University of Warwick, Coventry CV4 7AL, UK; D.J.Pascoe@warwick.ac.uk
Received 2017 August 10; revised 2017 September 15; accepted 2017 September 19; published 2017 September 28

Abstract

Quasi-periodic rapidly propagating wave trains are frequently observed in extreme ultraviolet observations of the solar corona, or are inferred by the quasi-periodic modulation of radio emission. The dispersive nature of fast magnetohydrodynamic waves in coronal structures provides a robust mechanism to explain the detected quasi-periodic patterns. We perform 2D numerical simulations of impulsively generated wave trains in coronal plasma slabs and investigate how the behavior of the trapped and leaky components depend on the properties of the initial perturbation. For large amplitude compressive perturbations, the geometrical dispersion associated with the waveguide suppresses the nonlinear steepening for the trapped wave train. The wave train formed by the leaky components does not experience dispersion once it leaves the waveguide and so can steepen and form shocks. The mechanism we consider can lead to the formation of multiple shock fronts by a single, large amplitude, impulsive event and so can account for quasi-periodic features observed in radio spectra.

Key words: magnetohydrodynamics (MHD) – shock waves – Sun: atmosphere – Sun: corona – Sun: oscillations – Sun: radio radiation

1. Introduction

The solar corona is a highly structured medium. Observations of the corona during eclipses using white light allowed the detection of rapidly propagating quasi-periodic waves (Williams et al. 2001, 2002; Katsiyannis et al. 2003). The spatial and temporal resolution provided by the *Solar Dynamics Observatory* Atmospheric Imaging Assembly now allow their detection in extreme ultraviolet (EUV) light (Liu et al. 2011, 2012). These disturbances are interpreted as fast magnetoacoustic waves (e.g., Cooper et al. 2003; Ofman et al. 2011) that are highly dispersive in coronal waveguides if their wavelength is comparable to the local width of the waveguide. An impulsive driver that generates a wide range of wavenumbers can therefore generate a quasi-periodic wave train some distance from the initial perturbation due to each wavenumber arriving at different times (Roberts et al. 1983, 1984). Numerical simulations (e.g., review by Pascoe 2014) have demonstrated that this behavior is a robust feature for coronal structures, for example, also being detected in models of current sheets (Jelínek & Karlický 2012; Jelínek et al. 2012) and observed above a fan structure (Mészárosová et al. 2013). Van Doorsselaere et al. (2016b) recently produced a review of other mechanisms that may be responsible for quasi-periodic pulsations (QPPs) in solar and stellar flares, while the statistical comparison of stellar and solar X-ray QPPs by Cho et al. (2016) supports a shared MHD wave mechanism for the modulation of emission.

Nakariakov et al. (2004) used wavelet transforms to analyze quasi-periodic wave trains and demonstrated that their time-dependent power spectrum produces a characteristic "crazy tadpole" signature. This signature was shown to be a robust feature of plane fast magnetoacoustic waveguides with different perpendicular profiles of the plasma density (Yu et al. 2015, 2016, 2017), and was found to be consistent with analytical estimations (Oliver et al. 2015). On the other hand, wavelet signatures of impulsively generated fast wave trains formed in cylindrical waveguides appear "head-first" (Shestov et al. 2015). The tadpole signature has been found in the spectra of rapidly propagating disturbances observed using white light (Katsiyannis et al. 2003; Nakariakov et al. 2004), and in EUV (Nisticò et al. 2014) which also allows spatial information about the wave trains to be measured (see also Yuan et al. 2013). Similar signatures are also frequently detected in post-flare radio emission (e.g., Mészárosová et al. 2009, 2016; Karlický et al. 2013), suggesting a common physical cause which is further supported by recent multi-wavelength studies such as the simultaneous detection of QPPs in hard X-ray, radio, and EUV bands (Kumar et al. 2016). Goddard et al. (2016) report the observation of a quasi-periodic wave train and shock-generated type II radio bursts having the same periodicity of approximately 1.8 minutes. Furthermore, a quasi-periodic pattern with a period drift consistent with a dispersively evolving fast wave train was very recently detected in radio emission (Kumar et al. 2017).

The behavior of fast magnetoacoustic wave trains in a funnel geometry has been modeled by Pascoe et al. (2013b, 2014) for both overdense waveguides and underdense anti-waveguides. In both cases, the leaky components form "wing" wave trains that propagate along, but outside, the magnetic funnel. This occurs due to the refraction produced by the expanding magnetic field, in contrast to straight waveguides for which the trapped and leaky components propagate in perpendicular directions. Typical relative amplitudes of rapidly propagating quasi-periodic compressive wave trains are observed to be lower than 5% (Liu et al. 2011). However, as the wave amplitude should increase with height, it is likely that the waves could experience nonlinear steepening in the higher regions of the corona. This steepening and associated acceleration of nonthermal electrons could be responsible for the QPPs in the radio emission detected after the wave trains (Goddard et al. 2016). The aim of this Letter is to study the effects of finite amplitude on the propagation of guided and leaky fast waves. The model equilibrium and perturbation are described in Section 2, and the results of our numerical simulations are presented in Section 3. Discussion of the application of our results to observations is presented in Section 4.

2. Model

The equilibrium magnetic field is taken to be straight, uniform, and aligned with the x-direction with strength B_0. A loop (or other waveguiding structure) is modeled as a field-aligned density enhancement using the general symmetric Epstein profile (e.g., Nakariakov & Roberts 1995; Pascoe et al. 2007a, 2007b, 2009)

$$\rho = (\rho_0 - \rho_e)\,\mathrm{sech}^2\left(\frac{y}{w}\right)^p + \rho_e, \quad (1)$$

where ρ_0 is the density at the loop axis, ρ_e is the density far from the loop, $p \geqslant 1$ determines the profile steepness, and w is the waveguide half-width. Simulations use $\rho_0/\rho_e = 4$ and $p = 8$ unless stated otherwise (see Figure 5). This steepness parameter closely approximates the step function profile in terms of wave behavior while remaining smooth and hence numerically well-resolved.

The uniform magnetic field provides a constant magnetic pressure $P_{\mathrm{mag}} = B_0^2/2\mu_0$ and so the structure is initially set in equilibrium by defining the internal energy density ϵ as

$$\epsilon = \frac{P_{\mathrm{gas}}}{\rho_0(\gamma - 1)}, \quad (2)$$

where P_{gas} is the (constant) gas pressure and $\gamma = 5/3$ is the ratio of specific heat capacities. The gas pressure is chosen to provide a low plasma $\beta = P_{\mathrm{gas}}/P_{\mathrm{mag}} = 0.05$, which is a typical value for the solar corona.

Simulations are performed using Lare2d (Arber et al. 2001), a 2.5D MHD code that solves the nonlinear MHD equations by performing a Lagrangian predictor-corrector time step and then remapping variables back onto the original Eulerian grid using van Leer gradient limiters. It is particularly well-suited to problems involving low-β plasmas and shocks, both of which are pertinent to our study.

Fast MHD waves are excited by applying a spatially localized compressive perturbation to the slab with the form

$$v_y = \frac{A_0}{\Delta_x \Delta_y} y \exp\left[-\left(\frac{x - x_0}{\Delta_x}\right)^2 - \left(\frac{y - y_0}{\Delta_y}\right)^2\right], \quad (3)$$

where A_0 is the initial amplitude, and the parameters Δ_x and Δ_y describe the width of the initial perturbation in the horizontal and vertical directions, respectively. To efficiently excite the fundamental modes we set the perpendicular spatial scale to be the slab width $\Delta_y = w = 1$ and also consider $\Delta_x = \Delta_y$ except when explicitly varied (see Figure 4). The perturbation is applied at the center of the numerical domain $x_0 = y_0 = 0$.

The 2.5D approximation used by Lare2d corresponds to $\partial/\partial z = 0$. Since v_z and B_z, associated with the Alfvén wave that is not considered in our study, remain zero due to our choice of initial conditions, our model is essentially 2D. A resolution of 8000×8000 grid points is used for all simulations. Convergence tests at a resolution of $16{,}000 \times 16{,}000$ grid points show no significant differences (e.g., the maximum amplitude of the perturbation changes by less than 1%). Line-tied boundary conditions were used, although our simulations end before the excited waves reach the boundaries. The numerical domain has a size of 300×300 in normalized units, i.e., 300 half-widths of the waveguide, which is converted to physical units by the choice of normalization constants. Physical length scales (X, Y), timescales (T), and speeds (V) are related to the dimensionless variables by $X = x\,w$, $T = t\,t_0$, and $V = v\,v_0$, where w, t_0, and v_0 are the chosen normalization constants for length scales, times, and speeds, and $v_0 = w/t_0$. For example, $v_0 = 1\,\mathrm{Mm\,s^{-1}}$, $t_0 = 1$ s, and hence $w = 1$ Mm. We note that the choice of normalization should be consistent with the MHD approximations. No kinetic effects such as Landau damping are considered in our model. We focus on the behavior of nonlinear MHD waves in terms of their capability to produce shock fronts that may generate radio bursts, but without directly modeling the associated particle acceleration.

3. Results

We perform numerical simulations for several values of perturbation amplitude given by Equation (3), which we designate according to the maximum value of the applied perturbation v_{y0} relative to the external Alfvén speed C_{Ae}. Figure 1 demonstrates our model setup. The top panel shows a snapshot of the density perturbation (i.e., with the density profile at $t = 0$ subtracted) at a time $t = 60$ after the initial perturbation for our largest amplitude simulation $v_{y0}/C_{\mathrm{Ae}} = 1.5$. The trapped components form two fast wave trains guided in the positive and negative x-directions and that have an extended spatial extent due to the effect of geometrical dispersion. The perturbations nearest to the origin correspond to the slow mode and propagate very slowly in our low-β plasma. The leaky components leave the loop and once outside propagate at the fast speed, which is mainly determined by the external Alfvén speed $C_{\mathrm{Ae}} = 1$ for our low-β plasma. The middle and bottom panels show snapshots of the density profile (we note not the density perturbation) demonstrating that the amplitude is sufficiently high that the guided sausage wave train noticeably perturbs the loop boundary. We also note that the slow mode at $x \approx 20$ has formed a shock, and the entropy mode can also be seen at $x = 0$.

Figure 2 shows the dependence of the maximum amplitude of the leaky wave train density perturbations, measured for propagation perpendicular to the equilibrium magnetic field. Each wave train attenuates as it propagates as a consequence of the expansion of the wave front. For lower amplitude perturbations, the behavior follows the $1/\sqrt{y}$ expected for an expanding, circular wave front created by a localized perturbation, while higher amplitudes experience additional attenuation due to nonlinear dissipation associated with the shock formation.

In comparison with the trapped wave trains, the leaky components travel at a greater speed, have a longer wavelength, and have a lower Q factor since they are dispersionless once in the external uniform plasma (this picture is different in the case of a structured external medium, e.g., the random structuring considered by Yuan et al. 2015). In terms of the signal measured at a fixed point some distance from the initial perturbation, the leaky components therefore have a longer period of oscillation than the trapped components that have a quasi-periodic signal at the same distance. A similar effect was modeled in coronal arcades by Hindman & Jain (2014). Both leaky and guided fast wave trains could be responsible for the rapidly propagating quasi-periodic compressive wave trains observed in the corona.

Figure 3 shows examples of the density perturbation signals measured at (37.5, 0), corresponding to the trapped wave

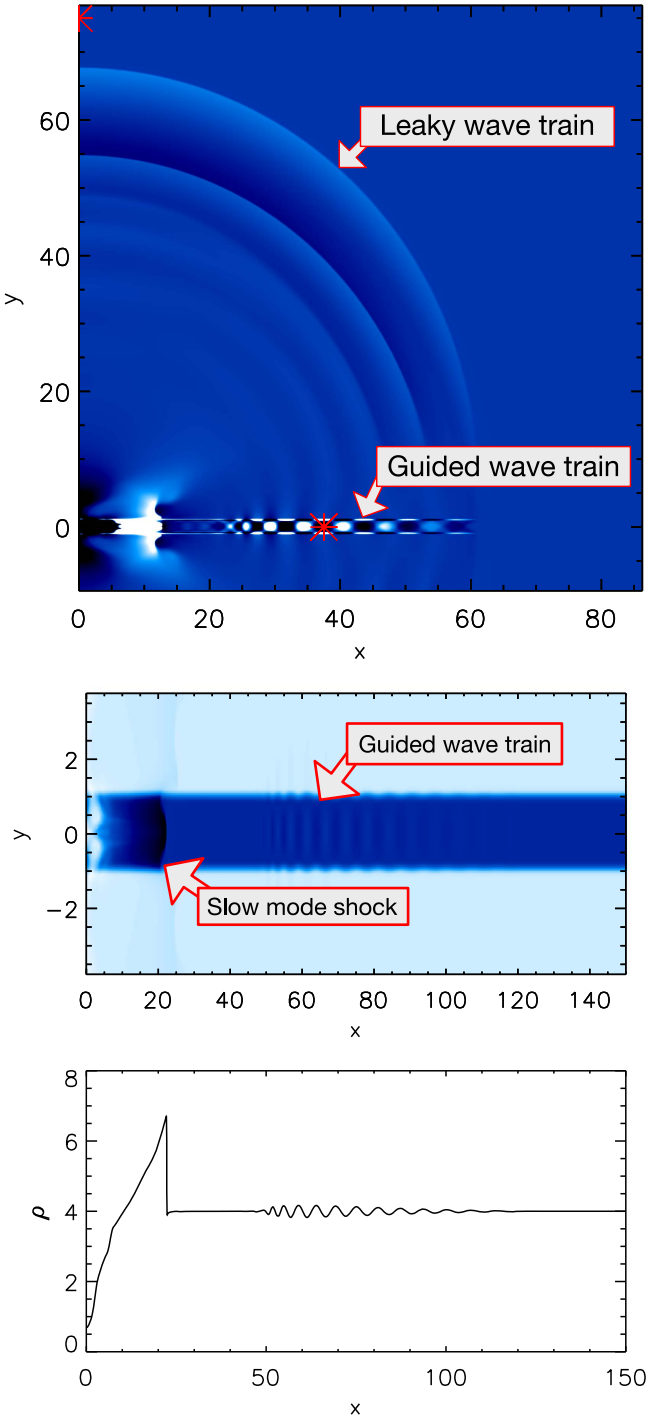

Figure 1. Snapshots of parts of the numerical domain for our largest amplitude simulation ($v_{y0}/C_{Ae} = 1.5$). The top panel shows the density perturbations at time $t = 60$. The red asterisks show the locations of the detection points for the trapped and leaky wave trains. The middle panel shows the density at time $t = 125$, with the profile at $y = 0$ also shown in the bottom panel.

trains, and at (0, 75), corresponding to the leaky wave trains propagating perpendicular to the slab axis. The results for three different amplitudes of the initial perturbation are shown: $A_0 = 0.01$, 0.5, and 3.5. The corresponding values of $v_{y0} = 0.004$, 0.30, and 1.50 are lower due the multiplicative y term in Equation (3) that generates the compressive (sausage) perturbation. For the trapped wave trains, the amplitude of the perturbations increases with the amplitude of the driver, but the

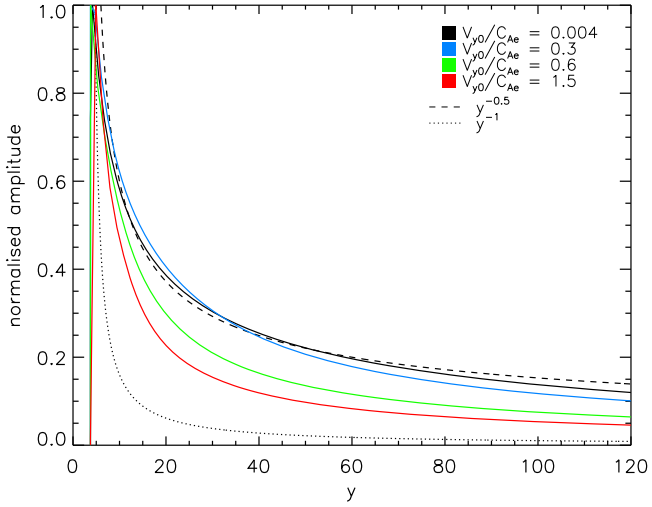

Figure 2. Dependence of the maximum amplitude of the leaky wave train measured at $x = 0$ on propagation distance y for different amplitudes of the initial perturbation.

wave trains are otherwise very similar. There is no sign of the nonlinear steepening that is readily apparent in the case of the leaky wave trains. The main difference between the trapped wave trains is the appearance of high-frequency oscillations at $t \gtrsim 95$ that increase with v_{y0}. This demonstrates that the geometrical dispersion is strong enough to prevent the formation of shocks inside the waveguide even in cases when it is sufficiently large to cause the external (leaky components with longer wavelength) wave trains to steepen, and also for the less-dispersive slow mode to steepen (see Figure 1). We note that the attenuation of the external wave train due to expansion in Figure 3 is approximately $75^{-1/2} \approx 0.12$, and so the leaky wave train amplitude upon leaving the slab is comparable to that of the trapped wave trains.

The leaky wave trains exhibit a similar number of oscillation cycles, as determined by the dispersive evolution experienced before the waves leave the slab. After this, no further geometrical dispersion occurs in the uniform external medium; however, the wave trains continue to evolve by nonlinear steepening, at a rate determined by the wave train amplitude relative to the local propagation speed (approximately the external Alfvén speed).

The amplitude of the external wave train upon just leaving the loop is determined not only by the initial perturbation but also the perpendicular density profile of the loop, i.e., the density contrast and steepness of the profile determine both the extent of the dispersive evolution and the fraction of wave energy that leaks away. It also depends on the relative spatial size of the initial perturbation with respect to the width of the waveguide (see Figure 4). Furthermore, the amplitude of the external wave train also continues to decrease as the wave front expands, here $\propto y^{-1/2}$ for the (approximately) circular front.

Figure 4 shows the results of simulations with $\Delta_x = 0.5$ (left panels), 1 (middle panels), and 2 (right panels). Changing the field-aligned width affects the spectral profile of the driver, i.e., the fraction of energy at each frequency. A larger Δ_x corresponds to a spatially broader (spectrally narrower) pulse and hence a more monochromatic wave train, as in Nakariakov et al. (2005), who considered the behavior of trapped wave trains in the linear regime. A similar dependence is also seen for the leaky wave trains, albeit to a much lesser extent,

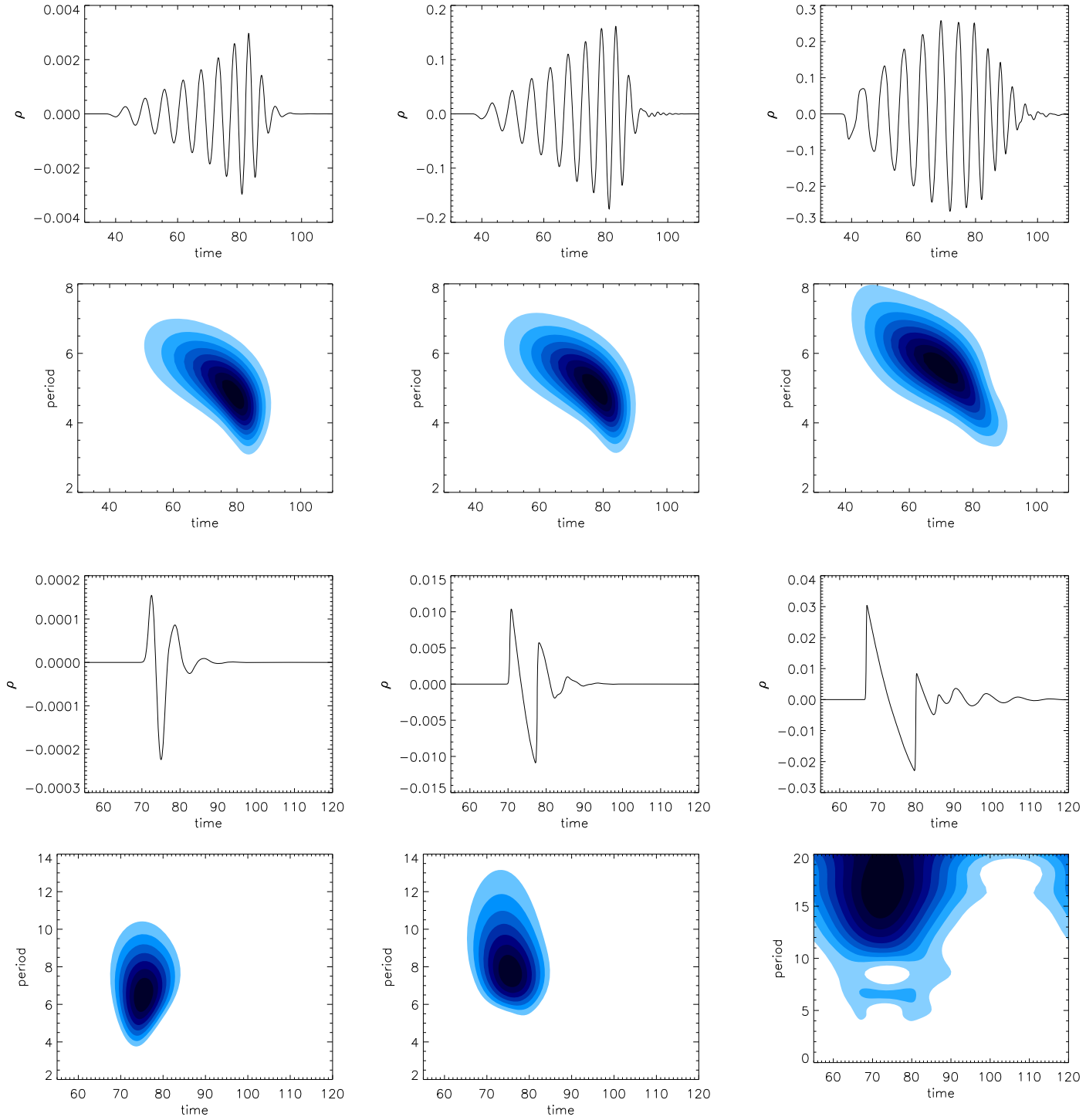

Figure 3. Density perturbations and wavelet analysis measured inside (top panels) and outside (bottom panels) the coronal slab. The applied perturbation amplitude v_{y0}/C_{Ae} is 0.004 (left), 0.30 (middle), and 1.50 (right).

mainly affecting the low-amplitude high-frequency components around $t = 85$ in the time series.

Figure 5 shows the results of a simulation with steepness parameter $p = 3$, corresponding to a perpendicular density profile with a much smoother transition from the internal to external value. Varying the steepness affects the group speed of different spectral components and the cutoff wavenumber for the leaky regime (e.g., Nakariakov & Roberts 1995). However, these are found to only be small effects, with the signatures being almost identical to their equivalent ones in Figure 4.

4. Discussion and Conclusions

In a uniform medium, fast magnetoacoustic waves of finite amplitude are subject to nonlinear steepening that results in the formation of shocks. The distance at which the shock is formed depends on the initial wavelength and amplitude. We may consider a harmonic fast wave of period P and amplitude A, propagating across the magnetic field in a zero-β plasma. In the weakly nonlinear regime, its amplitude, for example, the perturbation of the velocity V in the direction of the wave

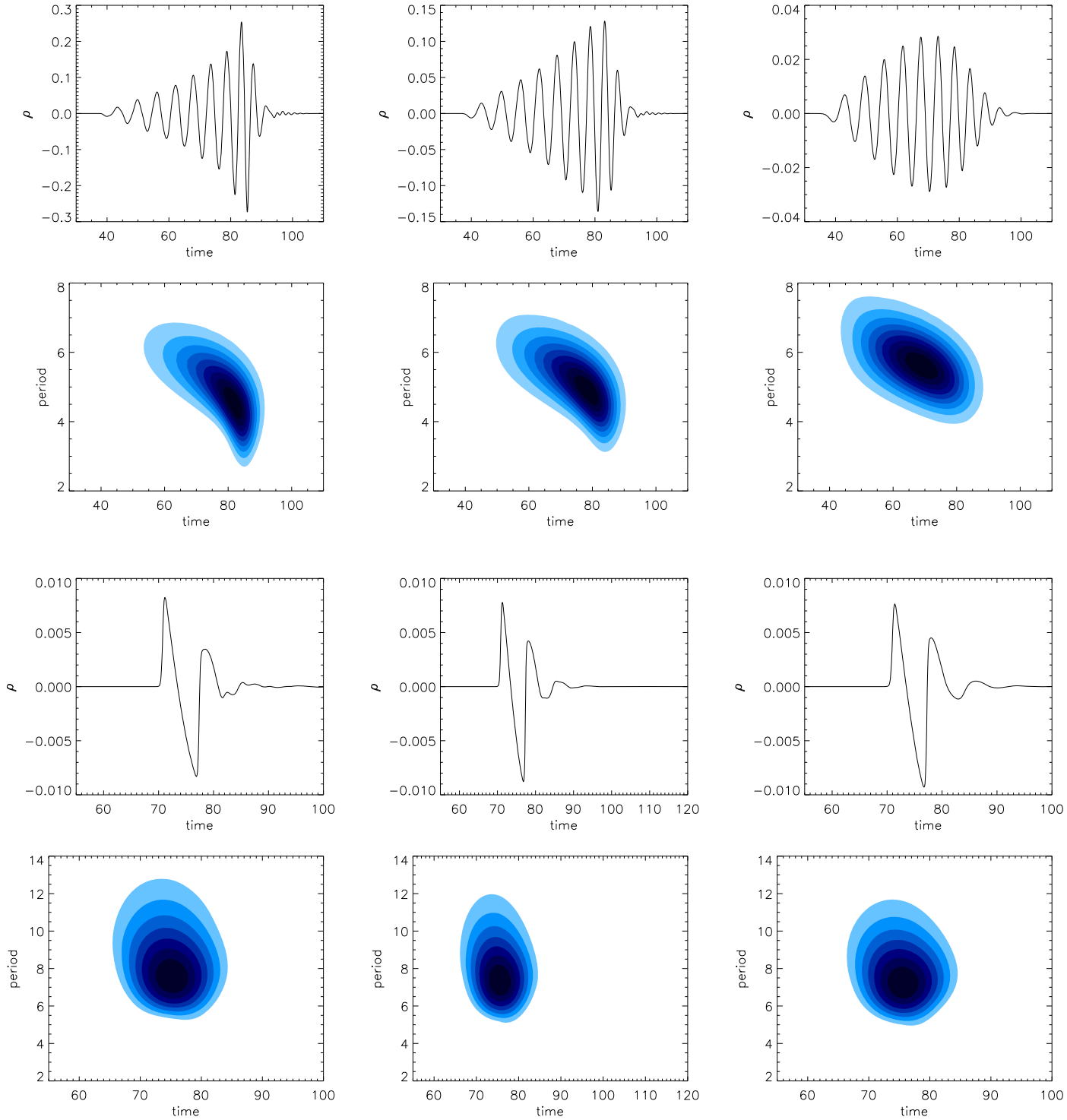

Figure 4. Dependence on the field-aligned spatial scale of the driver demonstrated by simulations with $\Delta_x = 0.5$ (left), 1 (middle), and 2 (right), with an applied perturbation amplitude $v_{y0}/C_{A0} = 0.21$ in all cases.

propagation, is described by

$$\frac{\partial V}{\partial t} + \frac{3}{2} V \frac{\partial V}{\partial \xi} = 0, \tag{4}$$

where ξ is the running coordinate connected with the coordinate along the direction of propagation y as $\xi = y - C_A t$, and C_A is the Alfvén speed. Equation (4) can be obtained, for example, from Equation (52) of Nakariakov et al. (2000) by taking $\mu = 0$, $C = C_A$, $C_s = 0$, and $\alpha = \pi/2$. The distance at which the shock forms can then be estimated as

$$x_{sh} \approx \frac{\lambda}{3\pi A}, \tag{5}$$

where λ is the wavelength and $\lambda = C_A P$. For example, a perpendicular fast wave of period 60 s in a uniform low-β plasma with Alfvén speed $C_A = 1\,\mathrm{Mm\,s^{-1}}$ forms a shock approximately 64 Mm from the excitation point for a

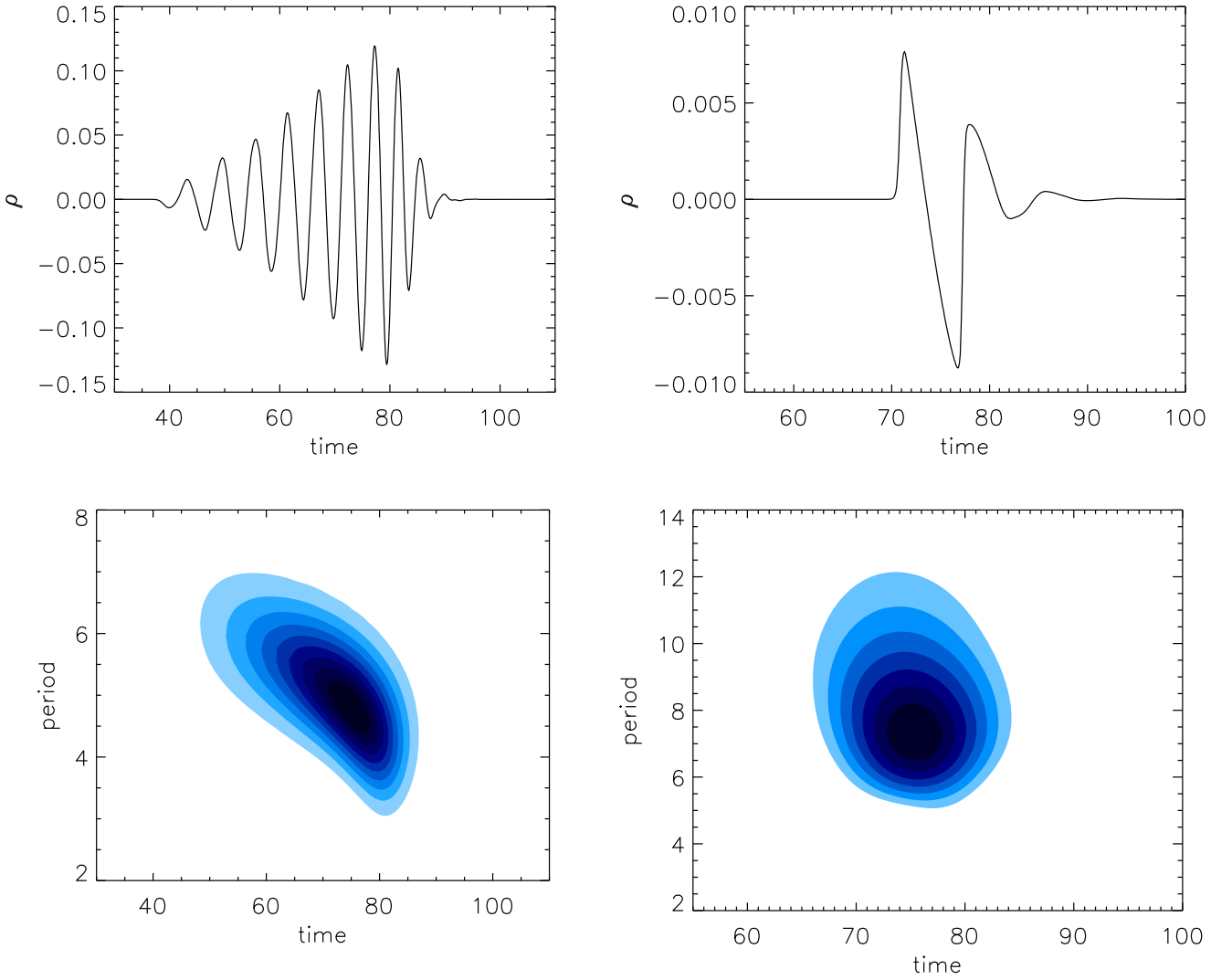

Figure 5. Density perturbations measured outside (left) and inside (right) the coronal slab with a steepness parameter $p = 3$.

normalized amplitude $A = 0.1$. Equivalently, the time between the impulsive event (e.g., solar flare) and the shock generation $t_{\rm sh}$ could be used to estimate the amplitude of the perturbation relative to the local Alfvén speed

$$A \approx \frac{P}{3\pi t_{\rm sh}}, \tag{6}$$

subject to additional geometrical effects being taken into account, i.e., this estimate corresponds to a plane wave. We note that for our model geometry, external wave trains with sufficient amplitude to steepen do so by the time they leave the loop, after which they mainly experience attenuation due to expansion and dissipation (see Figure 2). For our largest amplitude simulation we measure a velocity perturbation $V \sim 0.04\,{\rm Mm\,s^{-1}}$ after traveling approximately 56 Mm, implying an initial amplitude $V \sim 0.3\,{\rm Mm\,s^{-1}}$ (before attenuation by expansion). This gives $A \sim 0.3$ when normalized by the external Alfvén speed $C_{\rm A} = 1\,{\rm Mm\,s^{-1}}$, and so for the period $P \approx 6$ s we obtain a shock formation distance $x_{\rm sh} \approx 2.1$ Mm. This distance being $\sim w$ (and even an overestimate) is consistent with the leaky wave train having already shocked by the time it leaves the loop.

We can also apply the estimate above to the trapped waves in our simulations. Considering our largest amplitude simulation again, for the trapped wave train we measure a velocity perturbation $V \sim 0.05\,{\rm Mm\,s^{-1}}$, giving $A \sim 0.1$ when normalized by the internal Alfvén speed $C_{\rm A} = 0.5\,{\rm Mm\,s^{-1}}$ and with period $P \approx 6$ s. Accordingly, we obtain a shock formation distance $x_{\rm sh} \approx 3.2$ Mm, much less than the 37.5 Mm detection point used for our figures, but with no steepening evident in the signal.

We have therefore demonstrated that multiple shock fronts can be formed by a single impulsive event with a sufficiently large amplitude, such as a solar flare. The geometrical dispersion provided by coronal structures is required to generate quasi-periodic wave trains. On the other hand, the dispersion also efficiently suppresses nonlinear steepening in the trapped wave train, and so the formation of shocks is prevented inside the waveguide. This mechanism can therefore account for the observation of quasi-periodic type II radio bursts after a flare or coronal mass ejection, and particularly those with a similar periodicity to a wave train observed in EUV such as the recent observations by Goddard et al. (2016) and Kumar et al. (2017). However, it is necessary to appreciate that the shocks will be generated by the leaky components of the impulsively generated wave trains and to distinguish

whether any imaged wave train also corresponds to the leaky or the trapped components, or if both are observed as in Nisticò et al. (2014).

In comparison with standing kink oscillations of coronal loops, the seismological techniques based on quasi-periodic propagating wave trains are far less advanced. For example, previous studies and this Letter demonstrate how the particular shape of the (trapped and leaky) wave trains, or its appearance in wavelet analysis, depends on the density profile of the loop. However, no simple inversion technique currently exists to determine the density profile parameters from the measured oscillation. For this reason multi-mode observations would be particularly informative. Observations of standing kink oscillations have recently been used to calculate the density (and Alfvén speed) profiles for coronal loops using their damping profiles by resonant absorption (Pascoe et al. 2013a, 2016, 2017a, 2017c). The perpendicular inhomogeneity size has also been independently estimated by forward modeling the EUV intensity (Goddard et al. 2017; Pascoe et al. 2017b), although so far this has relied on the isothermal approximation (e.g., Aschwanden et al. 2007), whereas hot (multi-thermal) flaring loops may require more sophisticated forward modeling (e.g., De Moortel & Bradshaw 2008; Van Doorsselaere et al. 2016a). Simultaneous observations of standing kink oscillations would therefore allow the density profile to be seismologically inferred, allowing a much narrower parametric study to determine the properties of the driver (e.g., A, Δ_x) required to reproduce the observed wave trains and/or radio bursts.

This work is supported by the European Research Council under the *SeismoSun* Research Project No. 321141 (D.J.P., C.R.G., V.M.N.) and the STFC consolidated grant ST/L000733/1 (V.M.N.). The authors thank J. S. Bright and J. A. Fawcett for their contributions.

Software: Lare2d (Arber et al. 2001).

ORCID iDs

D. J. Pascoe https://orcid.org/0000-0002-0338-3962
C. R. Goddard https://orcid.org/0000-0003-0240-0465
V. M. Nakariakov https://orcid.org/0000-0001-6423-8286

References

Arber, T., Longbottom, A., Gerrard, C., & Milne, A. 2001, JCoPh, 171, 151
Aschwanden, M. J., Nightingale, R. W., & Boerner, P. 2007, ApJ, 656, 577
Cho, I.-H., Cho, K.-S., Nakariakov, V. M., Kim, S., & Kumar, P. 2016, ApJ, 830, 110
Cooper, F. C., Nakariakov, V. M., & Williams, D. R. 2003, A&A, 409, 325
De Moortel, I., & Bradshaw, S. J. 2008, SoPh, 252, 101
Goddard, C. R., Nisticò, G., Nakariakov, V. M., Zimovets, I. V., & White, S. M. 2016, A&A, 594, A96
Goddard, C. R., Pascoe, D. J., Anfinogentov, S., & Nakariakov, V. M. 2017, A&A, 605, A65
Hindman, B. W., & Jain, R. 2014, ApJ, 784, 103
Jelínek, P., & Karlický, M. 2012, A&A, 537, A46
Jelínek, P., Karlický, M., & Murawski, K. 2012, A&A, 546, A49
Karlický, M., Mészárosová, H., & Jelínek, P. 2013, A&A, 550, A1
Katsiyannis, A. C., Williams, D. R., McAteer, R. T. J., et al. 2003, A&A, 406, 709
Kumar, P., Nakariakov, V. M., & Cho, K.-S. 2016, ApJ, 822, 7
Kumar, P., Nakariakov, V. M., & Cho, K.-S. 2017, ApJ, 844, 149
Liu, W., Ofman, L., Nitta, N. V., et al. 2012, ApJ, 753, 52
Liu, W., Title, A. M., Zhao, J., et al. 2011, ApJL, 736, L13
Mészárosová, H., Dudík, J., Karlický, M., Madsen, F. R. H., & Sawant, H. S. 2013, SoPh, 283, 473
Mészárosová, H., Karlický, M., Rybák, J., & Jiřička, K. 2009, A&A, 502, L13
Mészárosová, H., Rybák, J., Kashapova, L., et al. 2016, A&A, 593, A80
Nakariakov, V. M., Arber, T. D., Ault, C. E., et al. 2004, MNRAS, 349, 705
Nakariakov, V. M., Mendoza-Briceño, C. A., & Ibáñez, S. M. H. 2000, ApJ, 528, 767
Nakariakov, V. M., Pascoe, D. J., & Arber, T. D. 2005, SSRv, 121, 115
Nakariakov, V. M., & Roberts, B. 1995, SoPh, 159, 399
Nisticò, G., Pascoe, D. J., & Nakariakov, V. M. 2014, A&A, 569, A12
Ofman, L., Liu, W., Title, A., & Aschwanden, M. 2011, ApJL, 740, L33
Oliver, R., Ruderman, M. S., & Terradas, J. 2015, ApJ, 806, 56
Pascoe, D. J. 2014, RAA, 14, 805
Pascoe, D. J., Anfinogentov, S., Nisticò, G., Goddard, C. R., & Nakariakov, V. M. 2017a, A&A, 600, A78
Pascoe, D. J., Goddard, C. R., Anfinogentov, S., & Nakariakov, V. M. 2017b, A&A, 600, L7
Pascoe, D. J., Goddard, C. R., Nisticò, G., Anfinogentov, S., & Nakariakov, V. M. 2016, A&A, 589, A136
Pascoe, D. J., Hood, A. W., De Moortel, I., & Wright, A. N. 2013a, A&A, 551, A40
Pascoe, D. J., Nakariakov, V. M., & Arber, T. D. 2007a, A&A, 461, 1149
Pascoe, D. J., Nakariakov, V. M., & Arber, T. D. 2007b, SoPh, 246, 165
Pascoe, D. J., Nakariakov, V. M., Arber, T. D., & Murawski, K. 2009, A&A, 494, 1119
Pascoe, D. J., Nakariakov, V. M., & Kupriyanova, E. G. 2013b, A&A, 560, A97
Pascoe, D. J., Nakariakov, V. M., & Kupriyanova, E. G. 2014, A&A, 568, A20
Pascoe, D. J., Russell, A. J. B., Anfinogentov, S. A., et al. 2017c, A&A, in press (https://doi.org/10.1051/0004-6361/201730915)
Roberts, B., Edwin, P. M., & Benz, A. O. 1983, Natur, 305, 688
Roberts, B., Edwin, P. M., & Benz, A. O. 1984, ApJ, 279, 857
Shestov, S., Nakariakov, V. M., & Kuzin, S. 2015, ApJ, 814, 135
Van Doorsselaere, T., Antolin, P., Yuan, D., Reznikova, V., & Magyar, N. 2016a, FrASS, 3, 4
Van Doorsselaere, T., Kupriyanova, E. G., & Yuan, D. 2016b, SoPh, 291, 3143
Williams, D. R., Mathioudakis, M., Gallagher, P. T., et al. 2002, MNRAS, 336, 747
Williams, D. R., Phillips, K. J. H., Rudawy, P., et al. 2001, MNRAS, 326, 428
Yu, H., Li, B., Chen, S.-X., & Guo, M.-Z. 2015, ApJ, 814, 60
Yu, H., Li, B., Chen, S.-X., Xiong, M., & Guo, M.-Z. 2016, ApJ, 833, 51
Yu, H., Li, B., Chen, S.-X., Xiong, M., & Guo, M.-Z. 2017, ApJ, 836, 1
Yuan, D., Pascoe, D. J., Nakariakov, V. M., Li, B., & Keppens, R. 2015, ApJ, 799, 221
Yuan, D., Shen, Y., Liu, Y., et al. 2013, A&A, 554, A144